ACS APPLIED MATERIALS & INTERFACES

Research Article

Cite This: ACS Appl. Mater. Interfaces 2018, 10, 12862−12869

www.acsami.org

Downloaded via UNIV OF NEBRASKA LINCOLN on February 20, 2019 at 23:04:54 (UTC).
See https://pubs.acs.org/sharingguidelines for options on how to legitimately share published articles.

Control of Synaptic Plasticity Learning of Ferroelectric Tunnel Memristor by Nanoscale Interface Engineering

Rui Guo,[†,‡] Yaxiong Zhou,[§] Lijun Wu,[∥] Zhuorui Wang,[§] Zhishiuh Lim,[‡] Xiaobing Yan,[†] Weinan Lin,[†] Han Wang,[†] Herng Yau Yoong,[†] Shaohai Chen,[†] Ariando,[‡,⊥] Thirumalai Venkatesan,[†,‡,⊥,#] John Wang,[†] Gan Moog Chow,[†] Alexei Gruverman,[¶] Xiangshui Miao,[*,§] Yimei Zhu,[*,∥] and Jingsheng Chen[*,†,‡]

[†]Department of Materials Science and Engineering, National University of Singapore, 117575, Singapore

[‡]NUSNNI-Nanocore, National University of Singapore, 117411, Singapore

[§]Wuhan National Laboratory for Optoelectronics, School of Optical and Electronic Information, Huazhong University of Science and Technology, Wuhan 430074, China

[∥]Condensed Matter Physics & Materials Science Division, Brookhaven National Laboratory, Upton, New York, New York 11973, United States

[⊥]Department of Physics, National University of Singapore, 117542, Singapore

[#]Department of Electrical and Computer Engineering, National University of Singapore, 117583, Singapore

[¶]Department of Physics and Astronomy, University of Nebraska−Lincoln, Lincoln, Nebraska 68588, United States

Supporting Information

ABSTRACT: Brain-inspired computing is an emerging field, which intends to extend the capabilities of information technology beyond digital logic. The progress of the field relies on artificial synaptic devices as the building block for brainlike computing systems. Here, we report an electronic synapse based on a ferroelectric tunnel memristor, where its synaptic plasticity learning property can be controlled by nanoscale interface engineering. The effect of the interface engineering on the device performance was studied. Different memristor interfaces lead to an opposite virgin resistance state of the devices. More importantly, nanoscale interface engineering could tune the intrinsic band alignment of the ferroelectric/metal−semiconductor heterostructure over a large range of 1.28 eV, which eventually results in different memristive and spike-timing-dependent plasticity (STDP) properties of the devices. Bidirectional and unidirectional gradual resistance modulation of the devices could therefore be controlled by tuning the band alignment. This study gives useful insights on tuning device functionalities through nanoscale interface engineering. The diverse STDP forms of the memristors with different interfaces may play different specific roles in various spike neural networks.

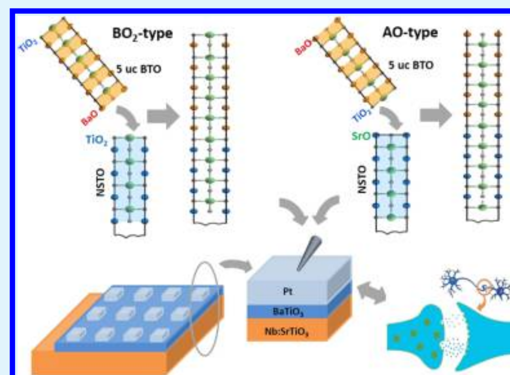

KEYWORDS: *ferroelectric tunnel junctions, memristor, nanoscale interface engineering, synapse, spike-timing-dependent plasticity*

INTRODUCTION

The quest for new computing technologies has triggered intense research into new materials and novel device architectures. In recent years, ferroelectric tunnel junctions (FTJs) have been studied extensively because of their potentials for nonvolatile binary data storage media.[1−8] An FTJ is a tunnel junction which has a simple structure with metal/ferroelectric barrier/metal. The electrical resistance of an FTJ is strongly dependent on the polarization orientation of the ultrathin ferroelectric film, which is called the tunneling electroresistance (TER) effect. Because the electrical resistance is coupled to ferroelectric polarization, FTJ provides a simple nondestructive reading method with relaxed constraint on the capacitor size, which overcomes the disadvantages of conventional ferroelectric random-access memory.[5] In addition to these, very recently, interesting memristive characteristics have been reported in FTJs,[9−13] which extend their great potentials of being used in newly emerged brain-inspired computing devices.

As an emerging field, brain-inspired technologies aim to extend the capabilities of information technology beyond the digital logic. In this field, an artificial synaptic device is utilized as the building block for brainlike computing systems to modulate the changes of synaptic connection weight (or strength).[14−17] A synapse is essentially a two-terminal device which resembles strikingly a memristor. Similar to the synaptic plasticity of a biological synapse, the conductance of a memristor could be tuned continuously based on the history of applied voltage or current.[18] Moreover, memristive devices

Received: January 28, 2018
Accepted: March 26, 2018
Published: March 26, 2018

© 2018 American Chemical Society

DOI: 10.1021/acsami.8b01469
ACS Appl. Mater. Interfaces 2018, 10, 12862−12869

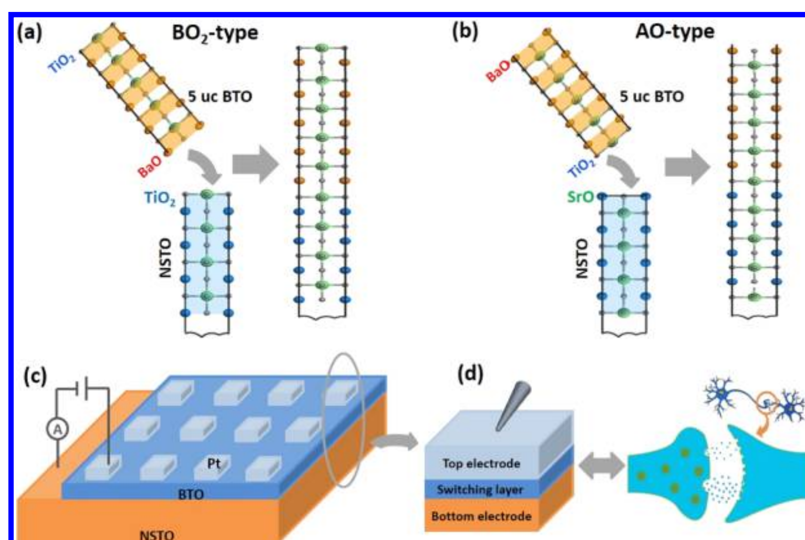

Figure 1. Schematic drawing of five uc BTO thin films grown on (a) TiO_2-terminated (BO_2-type) and (b) SrO-terminated (AO-type) NSTO substrates. (c) Schematic drawing of the ferroelectric tunnel memristor structure. (d) Structural diagram of a two-terminal ferroelectric tunnel memristor and a schematic illustration of the concept of using a memristor as a synapse.

can be scaled down to nanoscale and offer nonvolatile, fast, and low-energy electrical switching.[14] Because of all of these properties, memristors are ideal building blocks for applications of nonvolatile memories and artificial synapse. For synaptic plasticity learning, spike-timing-dependent plasticity (STDP) is a very important memorization mechanism, which is often interpreted as the comprehensive learning rule for a synapse—the "first law" of synaptic plasticity.[19,20] It refers to the phenomenon that the precise control of the pre- and postsynaptic spike timings could significantly affect the sign and magnitude of long-term synaptic modification. As regarded as one important memorization mechanism, STDP function has been experimentally demonstrated in a wide variety of artificial synaptic devices.[21−25]

As a new type of memristor, FTJ exhibits great potential for the future electronic synapse because of its advantages, such as having higher operation speed than the biological counterpart and very low-energy consumption. Furthermore, unlike conventional resistive random-access memory (RRAM) and phase-change memory (PCM), electroforming process is not needed for an FTJ-based memristor. This characteristic is important because most of the forming processes results in a discrete and abrupt resistive transition during the SET or/and RESET process.[26−29] However, despite the significant potential of FTJs to be used as an electronic synapse device, progress to date has been mainly focused on its memristive mechanisms.[9−13] STDP was recently reported in $BiFeO_3$-based FTJs[30] and $BaTiO_3$ (BTO)-based multiferroic tunnel junction.[31] In their work, the memristive response of the junctions was correlated to the nucleation-dominated reversal of ferroelectric domains or induced by the coupling of the ferroelectric domain reversal and the interfacial spin state. In addition, the rich physical properties of oxide interfaces governing the device properties are generally strongly dependent on the interfacial band alignment. For example, interface engineering can change the work function of (Nb:)$SrTiO_3$ (NSTO)[32] and the band alignment in perovskite metal−semiconductor heterostructure, greatly.[33] Moreover, it has already been reported that the surface termination of the ferroelectric barrier layer in contact with the metal electrode critically affects the electroresistive properties of FTJs.[34] We therefore believe that the nanoscale interface engineering of FTJ devices would also affect their memristive behavior and thus their synaptic learning properties greatly, of which the study is still lacking.

In this work, we report that the synaptic plasticity learning properties of Pt/$BaTiO_3$/Nb:$SrTiO_3$ ferroelectric memristors can be controlled by the nanoscale interface engineering. Two different top and bottom interfaces were deliberately controlled in this study by using TiO_2-terminated NSTO substrate (BO_2-type) or SrO-terminated NSTO substrate (AO-type) and unit cell (uc) by uc epitaxial growth. The switching of BTO polarization generates two conductance states: low-resistance (ON) state when the polarization of BTO points down and high-resistance (OFF) state when the polarization of BTO points up.[35] Four STDP forms were demonstrated in both types of memristors. The FTJ interfaces have a significant influence on their performance. Different interfaces cause opposite virgin-resistance states of the memristive devices. Besides, nanoscale interface engineering could tune the intrinsic band alignment of the ferroelectric/metal−semiconductor heterostructure over a large range of 1.28 eV. The different band alignments eventually result in different resistive-switching processes. Bidirectional or unidirectional gradual resistance modulation behaviors could be controlled through the nanoscale device interface engineering.

■ RESULTS AND DISCUSSION

Single crystalline 0.5 wt % NSTO was used as the substrate as well as the bottom electrode in this study. BTO ultrathin films with a thickness of 5 uc (2 nm) were deposited on (001)-oriented NSTO substrate using a pulsed laser-deposition (PLD) technique. Two different types of top and bottom interfaces can be created in the heterostructure by tailoring the termination of NSTO substrates and uc by uc epitaxial growth of BTO. TiO_2-terminated NSTO substrate can be obtained through HF etching and thermal treatment, whereas SrO termination can be achieved by depositing 1 uc of SRO on TiO_2-terminated NSTO substrate. SRO (1 uc) will result in SrO termination automatically.[36,37] The schematics of 5 uc

DOI: 10.1021/acsami.8b01469
ACS Appl. Mater. Interfaces 2018, 10, 12862−12869

BTO grown on NSTO with different terminations are shown in Figure 1a,b. Reflection high-energy electron diffraction (RHEED) patterns before and after film growth as well as the intensity oscillations of the specular reflected beam during depositions are shown in Figure S1. The clear intensity oscillations of the BTO film indicate its layer-by-layer growth mode, providing the atomic-scale control of the top and bottom interfaces. After the deposition of BTO thin film, an array of 10 μm × 10 μm Pt top electrodes (15 nm thick) were patterned using the lift-off technique. Figure 1c shows the schematic of the Pt/BTO/NSTO devices, and Figure 1d illustrates of the concept of using a memristor as a synapse. To verify the different interfaces of the two types of ferroelectric tunnel memristors, electron energy loss spectroscopy (EELS) spectrum imaging in scanning transmission electron microscopy (STEM) mode was performed, as shown in Figure 2. Ba

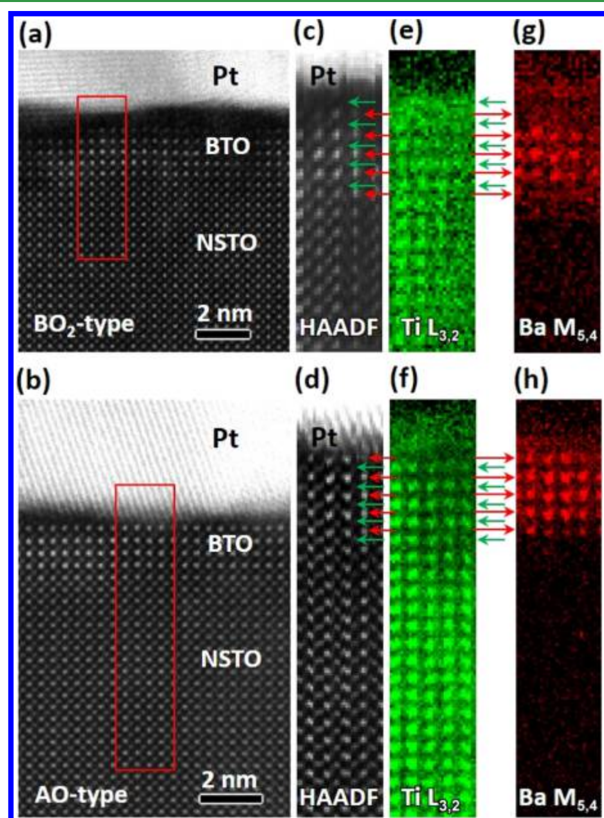

Figure 2. STEM results of BO_2- and AO-type devices. (a,b) HAADF images in STEM mode of BO_2- and AO-type device. EELS spectrum images with Ti $L_{3,2}$ edges and Ba $M_{5,4}$ edges from the area marked by a red rectangle area in (ab) were acquired. (c,d) Simultaneously acquired HAADF-STEM images of BO_2- and AO-type device during EELS spectrum image acquisition. (e−h) Ti $L_{3,2}$ (e,f) and Ba $M_{5,4}$ (g,h) signal intensity maps retrieved from the EELS spectrum image of BO_2- and AO-type devices after subtracting background. Ti and Ba atoms are clearly resolved in the EELS spectrum image mapping. Red and green arrows indicate the five layers of BaO and TiO_2, respectively.

and Ti atoms are clearly resolved in EELS mapping. From Ti $L_{3,2}$ (Figure 2e) and Ba $M_{5,4}$ (Figure 2g) signal intensity for BO_2-type device, there are five layers of BaO and TiO_2 as indicated by red and green arrows with the TiO_2 layer right below the Pt layer, indicating it is TiO_2-terminated on the surface. For the AO-type device, it is BaO layer right below Pt, indicating that it is BaO-terminated on the surface. Transmission electron microscopy results confirm the different top and bottom interfaces of the ferroelectric tunnel memristor devices grown on different terminated NSTO substrates. To test the ferroelectricity of the BTO barrier layer, piezoresponse force microscopy (PFM) and local hysteresis loops were measured, and the results are shown in Figure S2. BTO thin films grown on TiO_2- and SrO-terminated NSTO substrates have virgin states of downward and upward polarization, respectively, consistent with our earlier work.[38]

To compare the basic electron transport properties of the two types of ferroelectric tunneling memristors, their current−voltage ($I-V$) curves were measured at room temperature. Figure 3a,b shows the typical $I-V$ curves of BO_2- and AO-type memristors in the low-bias regime (−0.3−0.3 V), respectively. Because of the downward and upward virgin polarization states of BTO, the virgin state $I-V$ curves (pink color) of BO_2- and AO-type memristors reveal a tunneling ON and OFF state, respectively. Therefore, unlike conventional resistive switching based on redox reaction of metal oxides, electroforming process is not needed to achieve a stable resistive switching in two types of devices. After applying a bias of +4 or −7 V (1 ms) to the devices, the BTO polarization of the device was switched downward or upward regardless of its virgin state, and its corresponding $I-V$ curve displays a tunneling ON (purple) and OFF (yellow) state, respectively. It was found that the OFF-state $I-V$ curves of BO_2-type memristors always display an obvious diode effect, whereas the OFF-state $I-V$ curves of AO-type memristors are quite symmetric, as shown in Figure 3a,b, respectively. Different $I-V$ curve shapes of two types of memristors are also consistently revealed in their large-bias-range $I-V$ switching curves, as shown in Figure 3c,d, respectively. Clear resistive switching behaviors were observed in both types of memristors with the positive (negative) voltage leading to low (high) resistance state. To investigate the electron transport mechanism of the two types of memristors, $I-V$ curve fitting was performed (see Figure S3). It was found that the nonlinear ON-state $I-V$ curves within the small voltage range of the two types of memristors can be well-described by the direct tunneling (DT) theory, as shown in Figure 3a,b, respectively. As distinct from the ON-state $I-V$ data, OFF-state $I-V$ curves in Figure 3a,b could not be fitted reasonably by the DT theory, but by the Schottky thermionic emission instead (see fitting details in Figure S3). Different current transport mechanisms of BO_2- and AO-type memristors within different voltage ranges are summarized in Figure S3.

To further confirm the DT property of the ON state and the contribution of electron tunneling to the Schottky thermionic emission of the OFF state, the temperature-dependent $I-V$ curves were measured (see Figure S4). The ON-state $I-V$ curves show negligible temperature dependence, but the OFF-state forward currents show strong temperature dependence, consistent with the Schottky thermionic emission theory. The Schottky barrier height Φ_s of the OFF state at the BTO/NSTO interface can be estimated through fitting, which are 1.74 and 0.46 eV for BO_2- and AO-type tunneling devices, respectively (see details in Figure S4). Tuning the band alignment in the ferroelectric/metal−semiconductor heterostructure over a large range of 1.28 eV could therefore be achieved by tailoring the heterostructure interfaces. Two factors might contribute to the large difference of Φ_s. First, different interfaces could modify the band alignments of the heterostructure and therefore change the Schottky barrier height.[32,33] Second, based on the density functional theory calculation results in our former

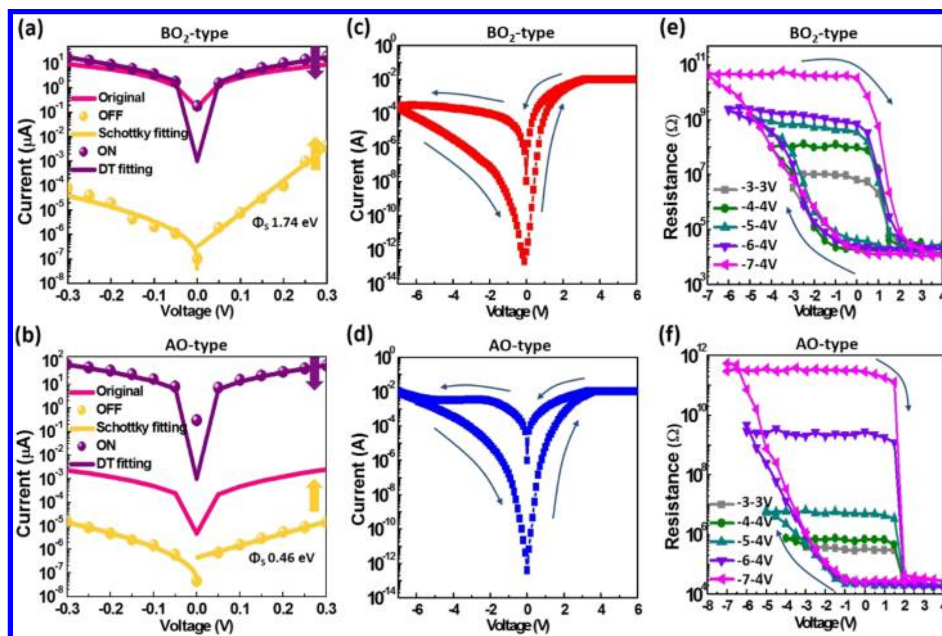

Figure 3. Basic properties of the ferroelectric tunnel memristor. (a,b) Typical $I-V$ curves in the low-bias region of BO_2- and AO-type memristor, respectively. The yellow and purple arrows represent upward and downward polarization of BTO, which correspond to the OFF and ON state of the memristive device, respectively. The yellow and purple dots (curves) show the $I-V$ data (fitted results) of the devices after a −7 or +4 V pulse (pulse width 1 ms) was applied. The pink color curves show $I-V$ date of the virgin states of the devices. (c,d) Typical $I-V$ switching curves of BO_2- and AO-type devices, respectively, which were measured by sweeping the voltage from −7 to 0, then 0 to 6, and finally back to −7 V. (e,f) Typical $R-V$ hysteresis loops of BO_2- and AO-type devices read at +0.2 V after applying different pulses with a pulse width of 1 ms.

work,[38] the binding energies of BTO/STO interfaces with different terminations differ significantly, which might also affect the band diagram and thus the Schottky barrier height.

To investigate the memristive switching behaviors of the two types of memristors, resistive memory loops ($R-V$ curves) were measured. Devices from five batches of BO_2- and AO-type memristive samples show a reproducible resistance change behavior with the typical results, as shown in Figure 3e,f. After applying a switching pulse with a pulse width of 1 ms, the resistance was read at a bias of +0.2 V. Both types of devices display a typical memristive behavior controlled by voltage pulses. A series of intermediate resistance states can be obtained by applying different voltage biases. When increasing the negative and positive switching voltage to −7 and +4 V, a giant ON/OFF ratio as large as 10^7 can be achieved for both types of FTJ devices (see details in Figure S5). The giant TER ratio of FTJs has already been reported by Xi et al.[39] The characteristic of a large ON/OFF ratio of memristive device is crucial because it increases the possibility of the memristor being used for the multilevel memory storage. The stability, retention, and endurance properties of the two types of memristive devices were also studied (see Figure S5). The results show high yield and good uniformity of the two types of memristive devices and indicate their long lifetime property. The memristive behavior of the Pt/BTO/NSTO junctions could be explained by a ferroelectric field-effect modulation on carrier concentration in the n-type semiconducting NSTO bottom electrode.[11] As shown in the $R-V$ curves, the resistance of the two types of devices could be modulated by a large negative bias (up to −7 V) without being saturated, which makes their $R-V$ switching loops asymmetric. We therefore believe that in addition to the ferroelectric polarization switching, drifting of oxygen vacancies under the negative electric field could also contribute to the observed giant ON/OFF ratios,[12,40−42] of which the mechanism is illustrated in Figure 4a,c. The accumulation of oxygen vacancies at the BTO/NSTO interface under the negative electric field will widen the depletion layer and consequently further enhance the electroresistance of the memristors. Note

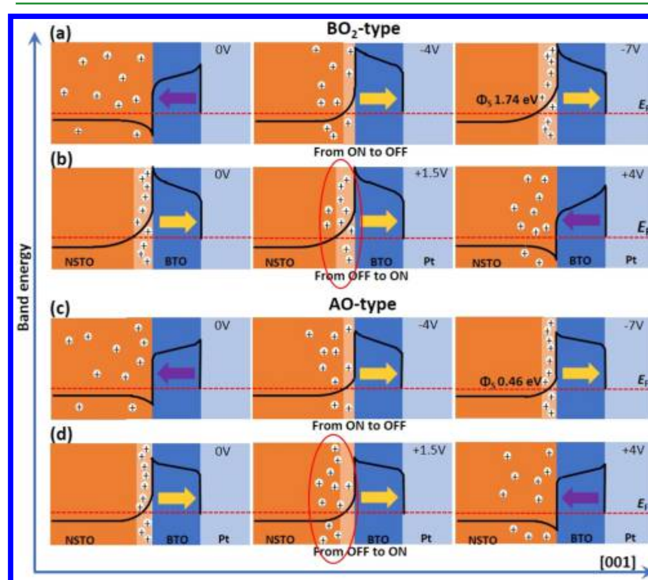

Figure 4. Schematic drawing of the resistive switching mechanism of two types memristive devices. (a,b) ON-to-OFF and OFF-to-ON resistive-switching processes of BO_2-type memristors. (c,d) ON-to-OFF and OFF-to-ON resistive-switching processes of AO-type memristors. The yellow arrow means the BTO polarization points toward Pt, whereas the purple arrow means the BTO polarization points toward NSTO. The red circle in (b,d) shows the oxygen vacancy detrapping process in two types of devices. The voltage was applied to the top Pt electrode, whereas the NSTO was grounded.

DOI: 10.1021/acsami.8b01469
ACS Appl. Mater. Interfaces 2018, 10, 12862−12869

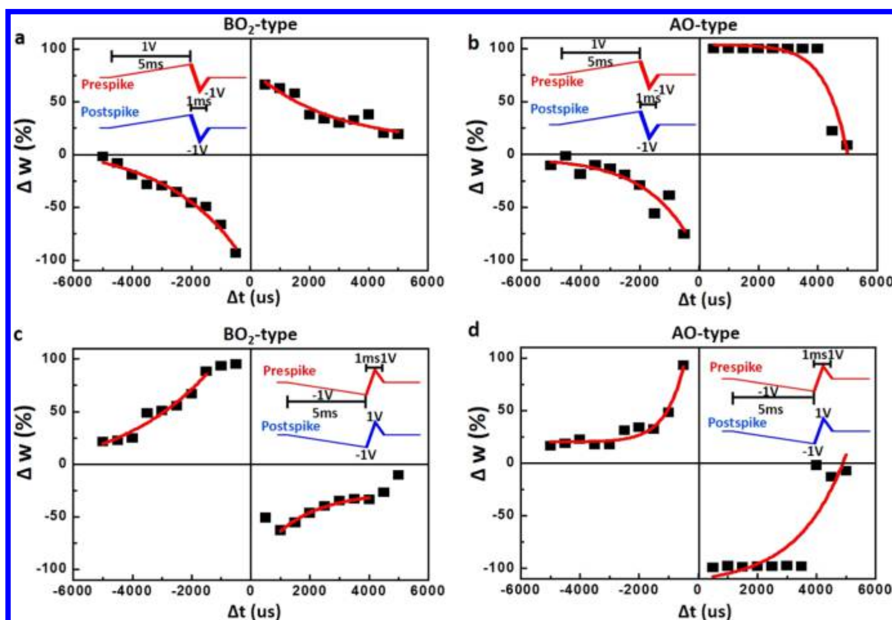

Figure 5. STDP properties of the two types of ferroelectric tunnel memristor. (a,b) STDP properties with typical antisymmetric Hebbian learning rule of BO_2- and AO-type memristors, respectively. (c,d) STDP properties with typical antisymmetric anti-Hebbian learning rule of BO_2- and AO-type memristors, respectively.

that the OFF-to-ON state transition of the AO-type memristors is very abrupt and sharp compared to that of the BO_2-type memristors. The different OFF-to-ON resistance switching processes of BO_2- and AO-type memristors are attributed to their different band alignments at the BTO/NSTO interfaces. As illustrated in Figure 4b, because of the large Schottky barrier at BTO/NSTO interface of the B-type memristors, the trapped oxygen vacancies could not detrap easily but migrate gradually with the increase of the positive bias. As a result, the slow oxygen vacancy detrapping process makes the OFF-to-ON state transition process gradual. In contrast, oxygen vacancies at BTO/NSTO interface of AO-type devices could detrap easily when a positive bias is applied because of its much smaller Schottky barrier (Figure 4b). Consequently, the sharpness of the OFF-to-ON resistive switching process of AO-type devices is mainly decided by the BTO polarization switching process. Because the trapped oxygen vacancies at the BTO/NSTO interface can detrap easily, as long as BTO is switched downward, the resistive OFF-to-ON switching process is then finished. To verify the oxygen vacancy migration under negative electric field, we measured the influence of pulse width on the resistive switching of the two types of memristors, and the results are shown in Figure S6. The results show that the ON/OFF ratio caused by BTO polarization switching is only around 10^3, but the migration of oxygen vacancies enhanced the ON/OFF ratio greatly on the order around 10^6. This is consistent with the fact that the virgin resistance of AO-type memristors is two or three orders of magnitude lower than the final OFF state obtained by applying −7 V (1 ms) (Figure 3b) because the virgin state does not involve the oxygen vacancy migration. Although the different resistive switching behaviors of the two types of memristors could be explained well by the model in Figure 4, we do not exclude other possible contributing factors, such as the influence of the top Pt/BTO interface and the effect of the interface roughness. Former studies imply that different Pt/BaO and Pt/TiO_2 interfaces might also affect the conduction properties of the ferroelectric junctions.[43,44] Besides, different roughness of Pt/BaO and Pt/TiO_2 interfaces might also affect the resistive switching of the two types of memristors.[45]

The different OFF-to-ON state transition behaviors of the two types of memristors imply their different synaptic properties. To emulate the synaptic weight modification, the pulse-driven conductance change of the two types of memristors was measured, and the typical results are shown in Figure S7. Consistent with the $R-V$ switching results, BO_2-type memristors display a bidirectional gradual conductance change, whereas AO-type memristors only realize unidirectional gradual conductance modulation. The ability of artificial synapses to possess bidirectional continuous conductance modulation is one essential prerequisite for applications in large neuromorphic network.[46] Up to now, although RRAM and PCM have been considered as promising candidates for synaptic devices, their shortcoming of discrete and abrupt resistive switching characteristic caused by the filament formation process prevents them from being utilized in large neural network systems. Therefore, the bidirectional continuous conductance modulation characteristic of BO_2-type ferroelectric tunnel memristor makes it suitable for most of the present neural network system. To further reveal the influence of the different band alignments on the synaptic properties of the two types of memristors, four STDP forms were measured. We apply a typical spike pairing protocol used in biological synaptic studies and in other electronic synapses to the memristors to emulate the pre- and postsynaptic activities. When pre- and postsynaptic spikes reach the memristor with a delay of Δt, their superposition produces a waveform which will induce the resistance change. Typical antisymmetric Hebbian learning rule and antisymmetric anti-Hebbian learning rule of BO_2- and AO-type ferroelectric memristors are shown in Figure 5a−d, respectively, with the insets showing the shapes of the applied pre- and postsynaptic spikes. Δw refers to the percentage change in synaptic weight, that is, the device conductance, representing the long-term nonvolatile modification of the synaptic efficacy as a function of the spike time interval Δt.[47] For antisymmetric Hebbian learning rule and

DOI: 10.1021/acsami.8b01469
ACS Appl. Mater. Interfaces 2018, 10, 12862−12869

antisymmetric anti-Hebbian learning rule, STDP can be simplified using an exponential function

$$\Delta w = A e^{-\Delta t/\tau} + \Delta w_0 \quad (1)$$

where A is the scaling factor, Δt is the time interval of the pre- and postsynaptic spikes, and τ is the time constant of the STDP function. Δw_0 is a constant which represents a nonassociative component of the synaptic change. As shown in Figure 5a,c for the antisymmetric Hebbian and anti-Hebbian rules of BO_2-type memristors, the change in the synaptic weight with the function of the spike-timing difference Δt could be well-fitted with the exponential functions, suggesting their good synaptic STDP characteristics. The large positive and negative maximum amount of synaptic modification reflects the very large window of the multiple memristive resistance status. In contrast, for AO-type memristors, there are abrupt changes of Δw in both learning rules when $\Delta t > 0$, as shown in Figure 5b,d. Symmetric Hebbian learning rule and symmetric anti-Hebbian learning rule of the two types of memristors were also measured (see Figure S8). BO_2-type memristors show good fitting of the two learning rules, whereas AO-type memristors also display abrupt changes in Δw. The different synaptic plasticity learning characteristics of the two types of devices are due to their gradual or abrupt conductance modulation property. The diverse STDP forms of the two types of memristors may play different specific roles in various spike neural networks (SNN). BO_2-type memristors could emulate biological synapses well with precise learning results, therefore can act as a decent artificial synapse in most of the present SNN. Nevertheless, in some specific cases, AO-type memristors might be preferred in the SNN when the synapse is required to learn easily but forget with much more difficulty. Control of the synaptic learning properties could therefore be realized by tuning the band alignments at the perovskite/semiconductor interface through tailoring the device interfaces.

CONCLUSIONS

In summary, synaptic plasticity learning property of the ferroelectric tunnel memristor could be controlled by the nanoscale interface engineering. Different interfaces of the devices result in different self-polarization directions of BTO thin films and thus the opposite ON or OFF virgin resistance state of the memristive devices. Nanoscale interface engineering could tune the intrinsic band alignment of the ferroelectric/metal−semiconductor heterostructure over a large range of 1.28 eV. The different band alignments result in different resistive switching processes. BO_2-type devices on TiO_2-terminated NSTO substrates possess bidirectional continuous conductance modulation characteristics. Gradual resistance modulation up to 10^7 could be achieved. In contrast, AO-type devices on SrO-terminated NSTO substrates only have unidirectional gradual conductance modulation characteristic. Bidirectional or unidirectional gradual resistance modulation behaviors of the two types of memristors lead to distinct different STDP properties. The synaptic learning properties could therefore be controlled by tuning the band alignments at the ferroelectric/semiconductor interface. Different STDP forms of the two types of memristors may play different specific roles in various SNNs. This study demonstrates the promising potentials of ferroelectric tunnel memristors for future synaptic device applications. Furthermore, our results provide essential insights into, and reference for, tailoring the electronic device functionalities by nanoscale interface engineering.

EXPERIMENTAL SECTION

Device Preparation. BTO thin films with different thickness of 5 uc were deposited by the PLD technique on NSTO substrates. NSTO substrates were treated before the film deposition. To get a TiO_2-terminated surface, a buffered HF acid-etching process was carried out, followed by a thermal treatment at 950 °C. The SrO termination was obtained by growing 1 uc of SRO layer on top of the treated TiO_2-terminated NSTO substrates using the SRO target. The 1 uc SRO layer was deposited with a substrate temperature of 750 °C and an oxygen pressure of 10 mTorr. BTO films were deposited at a substrate temperature of 600 °C with an oxygen partial pressure of 5 mTorr. After deposition, the films were cooled down to room temperature at an oxygen pressure of 100 Torr. The cooling rate was 5 °C/min till 300 °C, and then 10 °C/min to room temperature.

High-resolution STEM and EELS. High-resolution STEM−high-angle annular dark field (HAADF) imaging and electron diffraction were performed using the double aberration-corrected JEOL-ARM200CF microscope with a cold-field emission gun and operated at 200 kV. The microscope is equipped with JEOL and Gatan HAADF detectors for incoherent HAADF (*Z*-contrast) imaging, and Gatan GIF Quantum ER energy filter with dualEELS for EELS.

Piezoresponse Force Microscopy. The topography and ferroelectric polarization of the as-grown BTO films were characterized using PFM (Asylum Research MFP-3D) with Pt-/Ti-coated tips. The measurement was performed under contact mode with an ac voltage applied to the probe tip. The scan rate was kept at 0.5 μm/s.

Electrical Measurements. Two-point measurement method was used for the electrical measurement. The $I-V$ and $R-V$ curves were measured using a pA meter/direct current voltage source (Hewlett Package 4140B) on a low-noise probe station. The applied voltage is termed as positive (negative) if a positive (negative) bias is applied to the top Pt electrode. The switching pulses were applied using a pulse waveform generator (models PM8571/2A) and a picosecond pulse generator (model 10070A). The pulse-driven memristive behavior and STDP functions were measured by a home-built electrical characterization system containing a semiconductor characterization system (Keysight B1500A) with a pulse generator unit (Keysight B1525A HV-SPGU), a probe station (Cascade M150), and an oscilloscope (Agilent Technologies DSO7104B). The pulse generator integrated in the system has the specifications of pulse duration, rising time, and falling time, ranging from 10 ns to 1 s. Each portion of the segment pulse includes duration, rising time, and falling time, ranging from 20 ns to 1 s. The amplitude of applied pulses ranges from −5 to 5 V.

ASSOCIATED CONTENT

Supporting Information

The Supporting Information is available free of charge on the ACS Publications website at DOI: 10.1021/acsami.8b01469.

RHEED images/oscillations, PFM, $I-V$ fitting, stability and retention properties, pulse-width-dependent resistive switching measurements, pulse-driven memristive behavior, and symmetric Hebbian and anti-Hebbian learning rules results (PDF)

AUTHOR INFORMATION

Corresponding Authors

*E-mail: miaoxs@hust.edu.cn (X.M.).
*E-mail: zhu@bnl.gov (Y.Z.).
*E-mail: msecj@nus.edu.sg (J.C.).

ORCID

Rui Guo: 0000-0002-3733-8908
Yaxiong Zhou: 0000-0002-1445-5626
Gan Moog Chow: 0000-0001-7634-4553

Jingsheng Chen: 0000-0003-3188-2803

Notes

The authors declare no competing financial interest.

■ ACKNOWLEDGMENTS

The research is supported by the Singapore National Research Foundation under CRP award no. NRF-CRP10-2012-02 and IIP award no. NRF-IIP001-001. Work at Brookhaven National Laboratory was supported by the U.S. Department of Energy, Office of Basic Energy Science, Division of Materials Science and Engineering, under contract no. DESC0012704. J.C. is the member of the Singapore Spintronics Consortium (SG-SPIN).

■ REFERENCES

(1) Tsymbal, E. Y.; Gruverman, A. Ferroelectric Tunnel Junctions: Beyond the Barrier. *Nat. Mater.* **2013**, *12*, 602−604.

(2) Tsymbal, E. Y.; Kohlstedt, H. Tunneling Across a Ferroelectric. *Science* **2006**, *313*, 181−183.

(3) Gruverman, A.; Wu, D.; Lu, H.; Wang, Y.; Jang, H. W.; Folkman, C. M.; Zhuravlev, M. Y.; Felker, D.; Rzchowski, M.; Eom, C.-B.; Tsymbal, T. Y. Tunneling Electroresistance Effect in Ferroelectric Tunnel Junctions at the Nanoscale. *Nano Lett.* **2009**, *9*, 3539−3543.

(4) Chanthbouala, A.; Crassous, A.; Garcia, V.; Bouzehouane, K.; Fusil, S.; Moya, X.; Allibe, J.; Dlubak, B.; Grollier, J.; Xavier, S.; Deranlot, C.; Moshar, A.; Proksch, R.; Mathur, N. D.; Bibes, M.; Barthelemy, A. Solid-state Memories based on Ferroelectric Tunnel Junctions. *Nat. Nanotechnol.* **2012**, *7*, 101−104.

(5) Garcia, V.; Fusil, S.; Bouzehouane, K.; Vedrenne, S. E.; Mathur, N. D.; Barthélémy, A.; Bibes, M. Giant Tunnel Electroresistance for Non-destructive Readout of Ferroelectric States. *Nature* **2009**, *460*, 81−84.

(6) Yin, Y. W.; Burton, J. D.; Kim, Y.-M.; Borisevich, A. Y.; Pennycook, S. J.; Yang, S. M.; Noh, T. W.; Gruverman, A.; Li, X. G.; Tsymbal, E. Y.; Li, Q. Enhanced Tunnelling Electroresistance Effect due to a Ferroelectrically Induced Phase Transition at a Magnetic Complex Oxide Interface. *Nat. Mater.* **2013**, *12*, 397−402.

(7) Guo, R.; Wang, Z.; Zeng, S.; Han, K.; Huang, L.; Schlom, D. G.; Venkatesan, T.; Ariando; Chen, J. Functional Ferroelectric Tunnel Junctions on Silicon. *Sci. Rep.* **2015**, *5*, 12576.

(8) Guo, R.; Wang, Y.; Yoong, H. Y.; Chai, J.; Wang, H.; Lin, W.; Chen, S.; Yan, X.; Venkatesan, T.; Ariando; Gruverman, A.; Wu, Y.; Chen, J. Effect of Extrinsically Introduced Passive Interface Layer on the Performance of Ferroelectric Tunnel Junctions. *ACS Appl. Mater. Interfaces* **2017**, *9*, 5050−5055.

(9) Chanthbouala, A.; Garcia, V.; Cherifi, R. O.; Bouzehouane, K.; Fusil, S.; Moya, X.; Xavier, S.; Yamada, H.; Deranlot, C.; Mathur, N. D.; Bibes, M.; Barthélémy, A.; Grollier, J. A Ferroelectric Memristor. *Nat. Mater.* **2012**, *11*, 860−864.

(10) Yamada, H.; Garcia, V.; Fusil, S.; Boyn, S.; Marinova, M.; Gloter, A.; Xavier, S.; Grollier, J.; Jacquet, E.; Carrétéro, C.; Deranlot, C.; Bibes, M.; Barthélémy, A. Giant Electroresistance of Super-tetragonal $BiFeO_3$-Based Ferroelectric Tunnel Junctions. *ACS Nano* **2013**, *7*, 5385−5390.

(11) Wen, Z.; Wu, D.; Li, A. Memristive Behaviors in $Pt/BaTiO_3/Nb:SrTiO_3$ Ferroelectric Tunnel Junctions. *Appl. Phys. Lett.* **2014**, *105*, 052910.

(12) Hu, W. J.; Wang, Z.; Yu, W.; Wu, T. Optically Controlled Electroresistance and Electrically Controlled Photovoltage in Ferroelectric Tunnel Junctions. *Nat. Commun.* **2016**, *7*, 10808.

(13) Kim, D. J.; Lu, H.; Ryu, S.; Bark, C.-W.; Eom, C.-B.; Tsymbal, E. Y.; Gruverman, A. Ferroelectric Tunnel Memristor. *Nano Lett.* **2012**, *12*, 5697−5702.

(14) Yang, J. J.; Strukov, D. B.; Stewart, D. R. Memristive Devices for Computing. *Nat. Nanotechnol.* **2013**, *8*, 13−24.

(15) Prezioso, M.; Bayat, F. M.; Hoskins, B. D.; Adam, G. C.; Likharev, K. K.; Strukov, D. B. Training and Operation of an Integrated Neuromorphic Network based on Metal-Oxide Memristors. *Nature* **2015**, *521*, 61−64.

(16) Wang, Z.; Joshi, S.; Savel'ev, S. E.; Jiang, H.; Midya, R.; Lin, P.; Hu, M.; Ge, N.; Strachan, J. P.; Li, Z.; Wu, Q.; Barnell, M.; Li, G.-L.; Xin, H. L.; Williams, R. S.; Xia, Q.; Yang, J. J. Memristors with Diffusive Dynamics as Synaptic Emulators for Neuromorphic Computing. *Nat. Mater.* **2017**, *16*, 101−108.

(17) Kim, K.-H.; Gaba, S.; Wheeler, D.; Cruz-Albrecht, J. M.; Hussain, T.; Srinivasa, N.; Lu, W. A Functional Hybrid Memristor Crossbar-Array/CMOS System for Data Storage and Neuromorphic Applications. *Nano Lett.* **2012**, *12*, 389−395.

(18) Chua, L. Resistance Switching Memories are Memristors. *Appl. Phys. A* **2011**, *102*, 765−783.

(19) Shouval, H. Z.; Wang, S. S.-H.; Wittenberg, G. M. Spike Timing Dependent Plasticity: A Consequence of More Fundamental Learning Rules. *Front. Comput. Neurosci.* **2010**, *4*, 19.

(20) Ohno, T.; Hasegawa, T.; Tsuruoka, T.; Terabe, K.; Gimzewski, J. K.; Aono, M. Short-term Plasticity and Long-term Potentiation Mimicked in Single Inorganic Synapses. *Nat. Mater.* **2011**, *10*, 591−595.

(21) Jo, S. H.; Chang, T.; Ebong, I.; Bhadviya, B. B.; Mazumder, P.; Lu, W. Nanoscale Memristor Device as Synapse in Neuromorphic Systems. *Nano Lett.* **2010**, *10*, 1297−1301.

(22) Li, Y.; Zhong, Y.; Xu, L.; Zhang, J.; Xu, X.; Sun, H.; Miao, X. Ultrafast Synaptic Events in a Chalcogenide Memristor. *Sci. Rep.* **2013**, *3*, 1619.

(23) Alibart, F.; Pleutin, S.; Bichler, O.; Gamrat, C.; Serrano-Gotarredona, T.; Linares-Barranco, B.; Vuillaume, D. A Memristive Nanoparticle/Organic Hybrid Synapstor for Neuroinspired Computing. *Adv. Funct. Mater.* **2012**, *22*, 609−616.

(24) Krzysteczko, P.; Münchenberger, J.; Schäfers, M.; Reiss, G.; Thomas, A. The Memristive Magnetic Tunnel Junction as a Nanoscopic Synapse-Neuron System. *Adv. Mater.* **2012**, *24*, 762−766.

(25) Wang, Z. Q.; Xu, H. Y.; Li, X. H.; Yu, H.; Liu, Y. C.; Zhu, X. J. Synaptic Learning and Memory Functions Achieved Using Oxygen Ion Migration/Diffusion in an Amorphous InGaZnO Memristor. *Adv. Funct. Mater.* **2012**, *22*, 2759−2765.

(26) Waser, R.; Aono, M. Nanoionics-based Resistive Switching Memories. *Nat. Mater.* **2007**, *6*, 833−840.

(27) Liu, M.; Abid, Z.; Wang, W.; He, X.; Liu, Q.; Guan, W. Multilevel Resistive Switching with Ionic and Metallic Filaments. *Appl. Phys. Lett.* **2009**, *94*, 233106.

(28) Yang, J. J.; Pickett, M. D.; Li, X.; Ohlberg, D. A. A.; Stewart, D. R.; Williams, R. S. Memristive Switching Mechanism for Metal/oxide/metal Nanodevices. *Nat. Nanotechnol.* **2008**, *3*, 429−433.

(29) Waser, R.; Dittmann, R.; Staikov, G.; Szot, S. Redox-Based Resistive Switching Memories—Nanoionic Mechanisms, Prospects, and Challenges. *Adv. Mater.* **2009**, *21*, 2632−2663.

(30) Boyn, S.; Grollier, J.; Lecerf, G.; Xu, B.; Locatelli, N.; Fusil, S.; Girod, S.; Carrétéro, C.; Garcia, K.; Xavier, S.; Tomas, J.; Bellaiche, L.; Bibes, M.; Barthélémy, A.; Saïghi, S.; Garcia, V. Learning through Ferroelectric Domain Dynamics in Solid-State Synapses. *Nat. Commun.* **2017**, *8*, 14736.

(31) Huang, W.; Fang, Y.-W.; Yin, Y.; Tian, B.; Zhao, W.; Hou, C.; Ma, C.; Li, Q.; Tsymbal, E. Y.; Duan, C.-G.; Li, X. Solid-State Synapse Based on Magnetoelectrically Coupled Memristor. *ACS Appl. Mater. Interfaces* **2018**, *10*, 5649−5656.

(32) Susaki, T.; Makishima, A.; Hosono, H. Work Function Engineering via $LaAlO_3/SrTiO_3$ Polar Interfaces. *Phys. Rev. B: Condens. Matter Mater. Phys.* **2011**, *84*, 115456.

(33) Yajima, T.; Hikita, Y.; Minohara, M.; Bell, C.; Mundy, J. A.; Kourkoutis, L. F.; Muller, D. A.; Kumigashira, H.; Oshima, M.; Hwang, H. Y. Controlling Band Alignments by Artificial Interface Dipoles at Perovskite Heterointerfaces. *Nat. Commun.* **2015**, *6*, 6759.

(34) Yamada, H.; Tsurumaki-Fukuchi, A.; Kobayashi, M.; Nagai, T.; Toyosaki, Y.; Kumigashira, H.; Sawa, A. Strong Surface-Termination Effect on Electroresistance in Ferroelectric Tunnel Junctions. *Adv. Funct. Mater.* **2015**, *25*, 2708−2714.

DOI: 10.1021/acsami.8b01469
ACS Appl. Mater. Interfaces 2018, 10, 12862−12869

(35) Wen, Z.; Li, C.; Wu, D.; Li, A.; Ming, N. Ferroelectric-field-effect-enhanced Electroresistance in Metal/ferroelectric/semiconductor Tunnel Junctions. *Nat. Mater.* **2013**, *12*, 617−621.
(36) Yu, P.; Luo, W.; Yi, D.; Zhang, J. X.; Rossell, M. D.; Yang, C.-H.; You, L.; Singh-Bhalla, G.; Yang, S. Y.; He, Q.; Ramasse, Q. M.; Erni, R.; Martin, L. W.; Chu, Y. H.; Pantelides, S. T.; Pennycook, S. J.; Ramesh, R. Interface Control of Bulk Ferroelectric Polarization. *Proc. Natl. Acad. Sci. U.S.A.* **2012**, *109*, 9710−9715.
(37) Rijnders, G.; Blank, D. H. A.; Choi, J.; Eom, C.-B. Enhanced Surface Diffusion through Termination Conversion during Epitaxial $SrRuO_3$ Growth. *Appl. Phys. Lett.* **2004**, *84*, 505−507.
(38) Guo, R.; Shen, L.; Wang, H.; Lim, Z.; Lu, W.; Yang, P.; Ariando; Gruverman, A.; Venkatesan, T.; Feng, Y. P.; Chen, J. Tailoring Self-Polarization of $BaTiO_3$ Thin Films by Interface Engineering and Flexoelectric Effect. *Adv. Mater. Interfaces* **2016**, *3*, 1600737.
(39) Xi, Z.; Ruan, J.; Li, C.; Zheng, C.; Wen, Z.; Dai, J.; Li, A.; Wu, D. Giant Tunnelling Electroresistance in Metal/ferroelectric/semiconductor Tunnel Junctions by Engineering the Schottky Barrier. *Nat. Commun.* **2017**, *8*, 15217.
(40) Wang, L.; Zhang, Q.; Chang, L.; You, L.; He, X.; Jin, K.; Gu, L.; Guo, H.; Ge, C.; Feng, Y.; Wang, J. Electrochemically Driven Giant Resistive Switching in Perovskite Nickelates Heterostructures. *Adv. Electron. Mater.* **2017**, *3*, 1700321.
(41) Wu, S.; Luo, X.; Turner, S.; Peng, H.; Lin, W.; Ding, J.; David, A.; Wang, B.; Van Tendeloo, G.; Wang, J.; Wu, T. Nonvolatile Resistive Switching in $Pt/LaAlO_3/SrTiO_3$ Heterostructures. *Phys. Rev. X* **2013**, *3*, 041027.
(42) Cui, Y.; Peng, H.; Wu, S.; Wang, R.; Wu, T. Complementary Charge Trapping and Ionic Migration in Resistive Switching of Rare-Earth Manganite $TbMnO_3$. *ACS Appl. Mater. Interfaces* **2013**, *5*, 1213−1217.
(43) Stengel, M.; Vanderbilt, D.; Spaldin, N. A. Enhancement of Ferroelectricity at Metal−Oxide Interfaces. *Nat. Mater.* **2009**, *8*, 392−397.
(44) Chen, W. J.; Zheng, Y.; Luo, X.; Wang, B.; Woo, C. H. Ab Initio Study on the Size Effect of Symmetric and Asymmetric Ferroelectric Tunnel Junctions: A Comprehensive Picture with regard to the Details of Electrode/Ferroelectric Interfaces. *J. Appl. Phys.* **2013**, *114*, 064105.
(45) Mikheev, E.; Hoskins, B. D.; Strukov, D. B.; Stemmer, S. Resistive Switching and its Suppression in $Pt/Nb:SrTiO_3$ Junctions. *Nat. Commun.* **2013**, *5*, 3990.
(46) Yao, P.; Wu, H.; Gao, B.; Eryilmaz, S. B.; Huang, X.; Zhang, W.; Zhang, Q.; Deng, N.; Shi, L.; Wong, H.-S. P.; Qian, H. Face Classification using Electronic Synapses. *Nat. Commun.* **2017**, *8*, 15199.
(47) Froemke, R. C.; Dan, Y. Spike-timing-dependent Synaptic Modification Induced by Natural Spike Trains. *Nature* **2002**, *416*, 433−438.

DOI: 10.1021/acsami.8b01469
ACS Appl. Mater. Interfaces 2018, 10, 12862−12869